J Mater Sci: Mater Med (2012) 23:677–685
DOI 10.1007/s10856-012-4553-2

Qualitative assessment of microstructure and Hertzian indentation failure in biocompatible glass ionomer cements

Kun V. Tian · Peter M. Nagy · Gregory A. Chass · Pal Fejerdy · John W. Nicholson · Imre G. Csizmadia · Csaba Dobó-Nagy

Received: 28 March 2011 / Accepted: 11 January 2012 / Published online: 29 January 2012

Abstract Discs of biocompatible glass ionomer cements were prepared for Hertzian indentation and subsequent fracture analyses. Specifically, 2 × 10 mm samples for reproducing bottom-initiated radial fracture, complemented by 0.2 × 1 mm samples for optimal resolution with X-ray micro tomography (μCT), maintaining dimensional ratio. The latter allowed for accurate determination of volumetric-porosity of the fully cured material, fracture-branching through three Cartesian axes and incomplete bottom-initiated cracking. Nanocomputed tomography analyses supported the reliability of the μCT results. Complementary 2-dimensional fractographic investigation was carried out by optical and scanning electron microscopies on the larger samples, identifying fracture characteristics. The combined 3-D qualitative assessment of microstructure and fractures, complemented by 2-D methods, provided an increased understanding of the mechanism of mechanical failure in these cements. Specifically, cracks grew to link pores while propagating along glass-matrix interfaces. The methodological development herein is exploitable on related biomaterials and represents a new tool for the rational characterisation, optimisation and design of novel materials for clinical service.

1 Introduction

Glass ionomer cements (GICs), also called glass polyalkenoate cements, are the composite product of an acid–base reaction between an aqueous polymer solution and a glass powder [1]. They are widely used in dentistry [2, 3] and have also been considered for use in bone [4, 5] and ear reconstruction [6, 7] as well as in veterinary sciences [8, 9] for their good biocompatibility and bioactivity [3, 10] that stimulates tooth and bone remineralisation [11]. Their inherent adhesion to enamel, dentine and metal substrates [12, 13], among other advantages [14, 15], makes them ideal candidates for replacing silver amalgam and composite resins as biocompatible dental filling material [16]. However, current commercial GICs are brittle and simply

K. V. Tian · P. M. Nagy · I. G. Csizmadia · C. Dobó-Nagy (✉)
Materials Science Research Institute, Faculty of Dentistry, Semmelweis University, Szentkirályi Utca 47, 1088 Budapest, Hungary
e-mail: dobo@fok.usn.hu

K. V. Tian · G. A. Chass · I. G. Csizmadia
Global Institute of Computational Molecular and Materials Science (GIOCOMMS), Toronto, Canada

K. V. Tian · G. A. Chass · I. G. Csizmadia
Global Institute of Computational Molecular and Materials Science (GIOCOMMS), Budapest, Hungary

K. V. Tian · G. A. Chass · I. G. Csizmadia
Global Institute of Computational Molecular and Materials Science (GIOCOMMS), Beijing, China

G. A. Chass
Department of Biological and Chemical Sciences, Queen Mary University of London, London, UK

P. Fejerdy
Department of Prosthetic Dentistry, Faculty of Dentistry, Semmelweis University, Szentkirályi Utca 47, 1088 Budapest, Hungary

J. W. Nicholson
School of Science, University of Greenwich, Medway Campus, Chatham Kent ME4 4TB, UK

I. G. Csizmadia
Department of Chemistry, University of Toronto, Toronto, Canada

do not possess the toughness or mechanical strength requisite for load-bearing and large restorations [17]. Although the literature reports many studies elucidating the setting mechanism with the aim of improving the mechanical properties of GICs, there has been no significant improvement in their mechanical properties since their introduction in 1970s [1, 18–23].

Hertzian indentation, a mechanical test method with ball-on-disc geometry (reproducing tooth cusp compression into dental restoratives under mastication), has been proven to represent the failure behaviour of different types of dental restorative materials in the laboratory, particularly the clinically relevant failure mode (tensile failure on the lower surface) [24, 25]. Additionally, it complements more traditional mechanical characterisation methods, including tension [26], torsion, flexural [27] and compression tests [26, 28], while providing an additional material characteristics parameter.

This technique is further extended through fractographic analysis, which correlates strength test values with morphological properties of the fracture surface [29]. Fractographic analyses have been successfully applied to the studies of fracture surfaces of dental ceramics [30] and composite resins [29]. However, the imaging techniques adopted in these examinations limit the study to near-fracture surface regions, resulting in only partial detection of the three-dimensional (3-D) crack network; no information is revealed on internal defects and crack-microstructure interaction in the sample-bulk. Additionally, the high vacuum used in scanning electron microscopy causes dehydration, creating artificial features in the sample. Therefore, a non-destructive 3-D imaging method revealing structural features in the bulk of the material would be of considerable value. This has been made possible via recent developments in high-resolution X-ray computed tomography (μCT). Successful 3-D non-destructive fracture characterisation and microstructure analyses on engineering materials and bone cements have taken advantage of this technique [31, 32].

To the best of the authors' knowledge, this work represents the first ever 3-D assessment of failed dental materials. In the current paper, we explore the application of laboratory μCT as a tool for microstructural analysis and fracture assessment on Hertzian indentation samples of commercial dental GICs.

2 Materials and methods

Samples were prepared in two sizes: the quasi-standard size of Hertzian indentation samples at 2 mm thick × 10 mm diameter, complemented by miniature samples 0.2 mm thick × 1 mm diameter. The latter smaller size is of optimal resolution to enable thorough investigation by μCT, while maintaining the dimensional ratio of the larger samples. This geometrically similar arrangement proved to be mechanically comparable to the larger samples and fracture loads were found to be scaled with sample size.

2.1 Sample preparation

A conventional acid–base reaction setting GIC (0807231, Fuji IX capsule, GC, Tokyo, Japan) was used to prepare 10 pieces each of normal (2 × 10 mm) and miniature samples (0.2 × 1 mm) in purpose-made aluminium moulds. Following manufacturer's instructions, the capsule was shaken for 10 s in an amalgam mixer, followed by insertion of the capsule nozzle into the mould, itself coated with paraffin oil to act as a separation medium. Care was taken to firstly touch the mould wall with the nozzle and then raise it slowly as the paste was extruded into the mould until it was overfilled, in order to eliminate trapped air. A similarly-lubricated glass slab was then put on top of the mould and held in place for 2 min for initial setting to occur at 20 ± 2°C. The environmental humidity was not controlled, more closely reflecting the variability of application conditions. The sample was then de-moulded and wrapped tightly in aluminium foil to maintain water-balance, and subsequently stored in an incubator at physiologically relevant temperature of 37°C for 7 days.

2.2 Micro- and nano CT imaging and data analysis

The miniature samples were scanned before and after Hertzian indentation testing with X-ray microcomputed tomography (SkyScan 1172, Kontich, Belgium) using microfocused X-rays at 70 kV with a 0.5 mm thick Al filter. Micromorphological analyses were conducted on the scans using the instrument software (CTAn, SkyScan, Kontich, Belgium). Isometric voxel of 2 μm was used for image reconstruction. Segmentation of images at different gray levels was applied to visualise different phases of the samples by their different X-ray absorption. Due to the nonlinear character of absorption-density functions, pores were easily detected while the porosity characteristics were determined numerically. Although glass particles could be visualised, they could not be detected by the software. Three volume of interest (VOI, 0.2 mm thick × 0.3 mm diameter cylinders) of each sample were chosen for more detailed pore analyses. This involved determination of pore volume, surface area, surface/volume ratio, thickness and structure model index (SMI) - detected in the top layer (top 30 slices ≡ 60 μm), bottom layer (bottom 30 slices ≡ 60 μm) and in the whole volume of the sample, respectively. The grouped means of the top and bottom layer parameters were determined within each sample, with

all samples being subsequently compared using a student's *t* test at 95% confidence interval.

Two of the failed miniature samples were scanned with nanocomputed tomography (SkyScan 2011, Kontich, Belgium) using microfocused X-rays at 40 kV with no filter. An isometric voxel of 0.39 μm was used for image reconstruction. To assess the accuracy of the μCT results, three 20 nm thick × 200 nm diameter VOIs were chosen on both nano CT and μCT scans of the same sample for porosity parameter determination, with all results subsequently compared using a Student's *t* test at 95% confidence interval.

2.3 Hertzian indentation

Samples were tested resting freely on a 30% glass fibre-reinforced polyamide (nylon 6,6) (elastic modulus 10 GPa), substrate of 5 mm thick × 10 mm diameter, using a universal testing machine (Z005, 121-001609, Zwick, Ulm, Germany). With the aid of a computer connected microscope (1-747-034, dnt digital microscope camera, Conrad, Budapest, Hungary) for facilitating accurate alignment, loading was applied centrally on the sample through a 100Cr6 steel ball bearing of 20 mm diameter (2 mm for the smaller samples) at a crosshead speed of 0.2 mm min^{-1}. The load vs. displacement progression was monitored to determine the load-point of material failure. The test was terminated promptly upon observation of a sudden drop in load, with the maximum load attained utilised as the effective failure load.

2.4 Complementary imaging

The larger samples were examined after mechanical testing with an optical stereo microscope (Meiji, China) at up to 90× magnification, as well as with a scanning electron microscope (Hitachi S-2460N, Tokyo, Japan) at up to 1500× magnification, under vacuum.

3 Results and discussion

3.1 Hertzian indentation test

A representative force–displacement plot is shown in Fig. 1. The highest force the samples could sustain before failure was determined from the plots and the means determined from these values. The failure load for the normal samples was 218.7 ± 52.1 N; the value and variability being consistent with, and representative of, the diverse conditions of clinical preparation, application and setting. For the miniature samples, a value of 35.3 ± 1.0 N was recorded. The ratio of the failure load approaches that

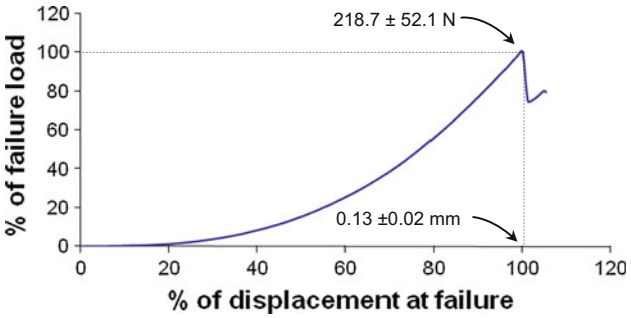

Fig. 1 Typical force–displacement plot resulting from Hertzian indentation test, presented as % of failure load as a function of % displacement at failure

of the geometrical dimensions, implying near-linear behaviour in failure load.

The scale of scatter in failure load for normal size samples was relatively high, yet is typical of the variability expected in practical and clinical applications. It is expected that flaws other than those inherent in the material would influence the strength of the samples. Determination of the fracture origin was therefore carried out in order to rationally characterise the observed failure behaviour and variability.

The failure behaviour of GICs is controlled by their composition as well as setting mechanism and kinetics. Conventional GIC setting occurs by an acid–base reaction. During setting, the outer layer of the glass is attacked by the acid, with unreacted glass cores bonding the carboxylic groups (COO^-) of the polyacid chains through ionic salt bridges with aluminium (Al^{3+}) and calcium cations (Ca^{2+}), both leached from the glass. The unreacted glass cores act as fillers within the resultant composite glass-polymer matrix [1].

Characterisation of Fuji IX is limited in the literature, with no Hertzian indentation tests reported to date. The values obtained in this study were in the range of those reported on other types of conventional GICs, in tests using the same sample geometry [25]. It is known that indentation size plays an important role in the failure mode of Hertzian indentation tests, hence can be controlled by choice of indenter size and sample thickness [33].

The present study used the same test geometry (2 mm thick × 10 mm diameter), and the samples were tested with a 20 mm diameter spherical indenter in a coating-substrate bi-layer structure, in order to reproduce bottom-surface initiated radial fracture which is the relevant clinical failure mode. During the indentation test, compression is generated on the top surface of the sample while tension builds at the bottom surface. For GIC samples of smaller thickness (2 mm), the intensity of the bottom tensile field for radial cracking is stronger than that of the top compressive field for cone cracking, hence, radial cracking

occurs first [25]. Due to instrumental limitation for initial crack detection, the test termination was slightly delayed (<1 s) after maximum load was reached (sample failure), extra compression work may have been applied to the samples. However, this does not affect failure load determination or principal crack recognition. More efficient means of crack detection, such as acoustic monitoring [25], will be applied in future work towards more effectively arresting the test once failure has occurred.

3.2 μCT imaging

Recent reports on pore distribution revealed that extrapolation of 2-D distributions to 3-D do not cover nor represent the real 3-D distribution. Specifically, synchrotron μCT investigations on small samples cut from impact-tested tantalum disks do not fit to the corrected 3-D distribution [34]. This finding indicates the importance and accuracy of the 3-D method. Representative pore parameters obtained by μCT are listed in Tables 1-2.

Our porosity data are in-line with previous works, wherein the porosity of the samples was $1.7 \pm 0.6\%$, fitting very well to the $0.06 \sim 2.99\%$ range previously published [35]. The porosity also varied along the depth of the samples, increasing from the top layer down through to the bottom layer, with the difference between the two layers being statistically significant at $P = 0.05$ within each sample (Table 1) and among all the samples (Table 2). This difference could be explained in part by elimination of some pores near the sample surface during the material curing process, but the scale of this difference indicated that other factors had also played a role.

All other determined shape parameters (Pore surface/volume ratio, Pore thickness, Structure SMI) indicated that the pores in the top layer were more elongated or flatter than those in the bulk and bottom layer of the sample. Pore size in the top layer was ~60–70% of pores in the whole volume and bottom layer, despite the fact that the surface tension in smaller pores has higher tendency to shape pores into spheres. The average pore thickness (smaller diameter) of the pores was two orders of magnitude smaller than the $0.25 \sim 1.15$ mm range previously reported [35]. This could be due to the collapse of large pores during preparation of miniature samples. To the best knowledge of the authors, such detailed pore characterisation has not been reported previously.

Based on the parameters obtained in this work it can be shown that the pore distribution was uneven throughout the whole sample volume; porosity and pore size increased on moving from the top, through the bulk, to the bottom with pore shape changing morphology from elongated to near-spherical. This phenomenon is attributed to the sample preparation technique, specifically through pressing of the sample top during curing. The glass slide used effectively forced out a portion of the entrapped air bubbles resulting in lower pore volume and irregular pore shapes in the top layer. This indicated that surface finishing, e.g. scraping and compressing, in clinical application may help to reduce the porosity and perhaps even improve material toughness; although some porosity is inevitable due to the mixing process. It is however unknown to what extent and magnitude the observed difference of pore morphology between the top and bottom layers influences the fracture procedure, as the difference in stress intensity between top and bottom surfaces determines the main failure mode.

Table 1 Mean values and standard deviations (in brackets) of porosity parameters as determined from three VOIs (0.2 mm thick × 0.3 mm diameter cylinders), for top and bottom layers and the whole volume of one representative miniature sample (0.2 × 1 mm)

	Pore volume (10^{-5} mm^3)	Porosity (%)	S:V[b] (10^3 mm^{-1})	Pore thickness (μm)	Structure SMI
Top layer	3.7 (1.5)[a]	1.2 (0.4)[a]	1.3 (0.1)[a]	5.0 (0.5)[a]	3.3 (0.0)
Bottom layer	12 (4.6)	3.1 (1.5)	0.9 (0.2)	8.5 (2.5)	3.8 (0.3)
Whole Volume	41 (11)	2.2 (0.5)	1.0 (0.2)	8.1 (2.3)	3.6 (0.3)

[a] The difference between the top layer value and bottom layer value was statistically significant at $P = 0.05$

[b] S:V—pore surface/volume ratio

Table 2 Mean values and standard deviations (in brackets) of porosity parameters as determined from three VOIs (0.2 mm thick × 0.3 mm diameter cylinders), for top and bottom layers and the whole volume of all miniature samples (0.2 × 1 mm)

	Pore volume (10^{-5} mm^3)	Porosity (%)	S:V[b] (10^3 mm^{-1})	Pore thickness (μm)	Structure SMI
Top layer	3.5 (1.3)[a]	1.1 (0.3)[a]	1.1 (0.3)[a]	6.4 (1.9)[a]	3.4 (0.3)
Bottom layer	8.5 (3.7)	2.5 (1.2)	0.8 (0.2)	9.0 (2.6)	3.9 (0.4)
Whole Volume	27.9 (14.1)	1.7 (0.6)	0.9 (0.2)	9.1 (2.5)	3.7 (0.3)

[a] The difference between the top layer value and bottom layer value was statistically significant at $P = 0.05$

[b] S:V—pore surface/volume ratio

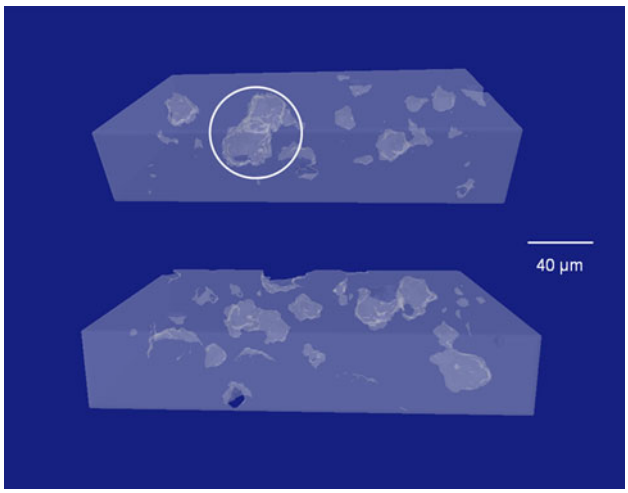

Fig. 2 MicroCT image of internal pore (*white*) and matrix (*light blue*) distribution. The upper piece represents a portion of the top layer (top 30 slices ≡ 60 μm), while the lower piece represent the bottom layer (bottom 30 slices ≡ 60 μm). Inter-connected pores near the surface of the top layer are circled (Color figure online)

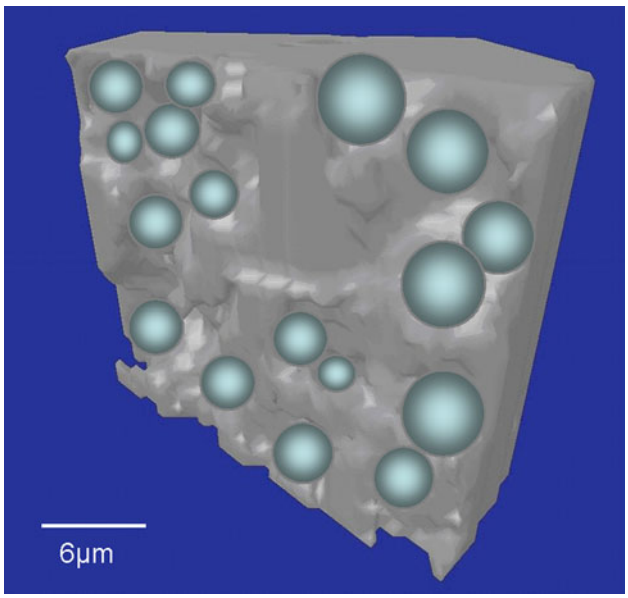

Fig. 3 MicroCT mapping of the radial fracture surface, wherein *greyish-cyan* spheres highlight the distribution of pores on the fracture-surface. *Dark grey* recesses and dimples highlight the pre-fracture location of glass cores from the opposing fracture face (Color figure online)

Figure 2 represents segmented X-ray tomography images from top and bottom layers of a sample, and shows that air and matrix phases are distinguishable. The air phase has significantly lower X-ray absorption than the matrix, allowing segmentation to reliably resolve pore distribution. The top layer shows reduced porosity with respect to the bottom layer, in agreement with the numerical results presented above. The irregular shape of the pores however may be related to the high viscosity as well as the short working and setting times of GICs (2 and 5 min, respectively [36]). Due to partial volume effects and the small difference in X-ray absorption between the glass cores and cement matrix, segmentation could not reliably resolve these two phases. SEM was used to complement the microstructure analyses of these two phases on the fracture surfaces.

As previously noted, fracture processes cannot be treated as 2-D phenomena, but instead as 3-D systems of branching cracks [37]; μCT imaging in 3-D facilitates imaging of such material failure. The size of the smaller samples used in this study (0.2 × 1.0 mm) was critical to the μCT resolution. Due to projection geometry of cone beam CTs, resolution varies inversely with sample diameter. Hence, the miniature sample size provides a compromise between optimal resolution and characteristic sample dimension and preparation. Figure 3 represents the 3-D microtomography of a portion of the fracture surface. Spheres are used to highlight the location of pores prior to crack propagation through them while the irregularly shaped recesses and dimples denote the sites where the glass cores from the opposing fracture-face were embedded in the matrix. The main crack propagated preferentially along the weak points of the material, specifically along the pores and the glass-matrix interfaces, implying filler-matrix binding is responsible for GICs' low fracture toughness.

Figure 4 shows the "pore phase" in a sample after the Hertzian indentation test, as determined through the μCT methodology, using the differing X-ray absorption of open cracks and pores, with respect to the absorption of the matrix. The tendency of microcracks to propagate through the pores in the vicinity of the crack path was observed while the crack propagating from the origin was deflected at a point of low porosity, changing direction to form a 'T-shaped' crack connecting the main cracks. This implied locally increased failure resistance by crack branching, as well as cracking being linked to sample inhomogeneity.

Partial radial cracking was also observed initiating from the sample's bottom surface. These were effectively arrested prior to reaching the top surface, and prevented from joining the main crack(s). These observations demonstrate the important contribution of the pore-crack interaction to the fracture process in GICs. The conclusion from these observations was that the mechanical properties of GICs could be improved through strengthening the glass-matrix bonding, eliminating (or at least reducing) porosity as well as increasing sample homogeneity.

The microtomography has resolution limitation of 4.4 μm, hence any smaller features were not resolved, including any fused pores (see Fig. 2). Instead, these appeared as a single feature.

The nano CT image in Fig. 5 presents the spatial relationship between the microcracks and the glass cores, as

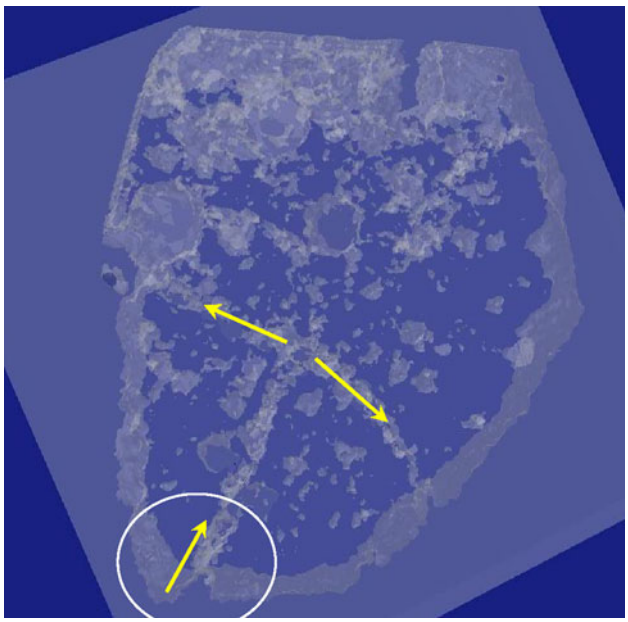

Fig. 4 Segmented microCT of one dissected piece of a fractured GIC sample, with the fracture origin oriented towards the bottom (*white circle*). The image shows the pores and pore-phase (*milky white*) linked by micro-cracks. The crack originating from the bottom progresses at a ~60° angle up and to the right (*single yellow arrow*), until it is deflected left–right, to form a 'T-shaped' crack (*yellow arrows*), effectively connecting the principal cracks and contributing to overall failure. The initial crack-arrest at the 'T-intersection' attests to the material failure being linked to sample inhomogeneity (Color figure online)

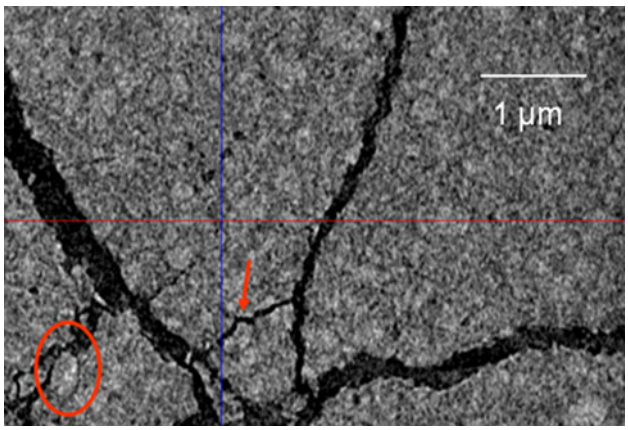

Fig. 5 Nano CT image showing that microcracks propagating along the interface of the matrix and glass cores (*arrow* and *oval*)

well as the microcracks propagated along the edges and sides of the glass cores (glass core-matrix interface). The effective porosity determined by nano CT (15.1 ± 4.0%) was higher than that of µCT (11.6 ± 0.1%), due to the inclusion of pores of thickness <4.4 µm that could not be resolved by µCT. As these values were not of significant statistical difference at $P = 0.05$, it is concluded that the method used in this study generates reliable results with respect to the high variability of material preparation in practical and clinical settings.

3.3 Complementary imaging

Conventional GICs are known to be brittle materials with high elastic modulus, and very low fracture toughness compared to composite resins [38]. The typical brittle fracture patterns such as hackles radiating out across the fracture surfaces from fracture origin, similar to those observed in glasses but in smaller scale [39], were observed in the optical (Fig. 6a) and scanning electron micrographs (Fig. 6b). As GICs are translucent, this presents pronounced difficulty for effective optical examination of their fracture surfaces. Through optimisation of illumination under optical microscope (transillumination) the fracture origin could be recognised. The SEM micrograph in Fig. 6b clearly reveals these radial hackles and enables the pinpointing of crack origin responsible for material failure. Nearly all recognised fracture origins were surface-exposed pores, or surface dimples created during sample preparation. The crack almost always initiated from these differently-sized recesses. Failure initiation by flaws was therefore shown to be independent of size, generating a relatively high scatter in failure load. SEM micrographs of the bottom surface of the samples also revealed extensive surface-exposed pores that may also act as fracture origins at differing loading conditions. This indicated that much effort should be put into increasing the surface quality of the restoration in practice, in order to obtain optimal material performance. This is in addition to the previously mentioned requirement for improving sample homogeneity.

No cone cracking nor plastic zone under the contact area was observed, confirming previous observations [25]. The smaller samples were not similarly examined by SEM. It was concluded that for the smaller samples radial cracking is also the primary failure mode, as in the standard dimension samples. Hence, it is deduced that the size of plastic zone has no significant effect even in this case.

Scanning electron micrographs of the fracture surface (Fig. 7) revealed extensive microcracks and porosity. The small and large pores distributed intermittently throughout the material were approximately at 13 µm and 26 ~ 28 µm in diameter, respectively. The microcracks preferentially linked the pores, propagating through the matrix and along the glass-matrix interface. The cement did not have well integrated surface texture and the angular glass cores appeared loosely bound to the polyacid matrix. Also the exposed glass cores had a defined smooth surface indicating that weak bonding between the glass cores and polyacid matrix was broken during the test. If this bond was strong enough the cracks would not propagate along the glass-matrix interface but would instead proliferate through the

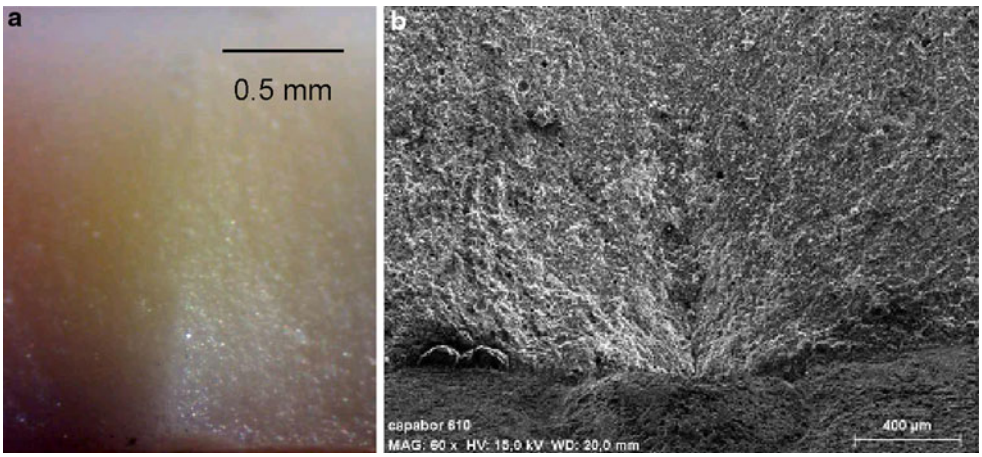

Fig. 6 **a** Optical image showing the fracture origin at the middle of the bottom surface, with hackles radiating out from the origin; **b** Scanning electron micrograph of the same specimen shows incomplete radial cracking, as well as the hackles that radiate out from the origin

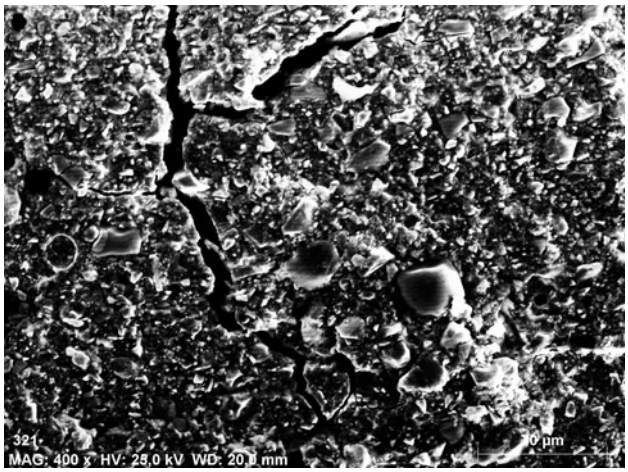

Fig. 7 Scanning electron micrograph of the fracture surface at 400× showing the glass cores exposed upon material fracture, with the microcrack propagating along the edge of the glass cores

matrix as well as the glass particles near or exposed to the surface in Fig. 7. However, a polymer layer should limit visibility of the latter. Some microcracks also preferentially propagated through the pores and were deflected at the glass cores, a tendency of cracks to avoid glass cores. The stress intensity difference between the top and bottom surfaces of the samples determined the failure mode and the microstructure and porosity locally influenced crack propagation direction. These observations are in direct agreement with the μCT observation for the fracture procedure assessment.

The high vacuum used in SEM could have changed the surface morphology, as well as caused some of the microcracks in the samples. GICs are known to contain loosely bonded water in their structure [21] which would evaporate in vacuo. This explains the observation that translucent samples turned chalky after SEM examination. This problem is avoided in the μCT imaging used in this study, as it is carried out under conditions of ambient pressure and temperature, mimicking the conditions of real practical applications and clinical use of GICs.

4 Conclusions

Laboratory X-ray micro tomography (μCT) has been shown to provide a high resolution 3-D image of the bulk of the glass ionomer dental materials before and after Hertzian indentation testing that resulted in material failure through cracking. This non-destructive technique producing high-resolution images is appropriate for microstructure characterisation and fracture-microstructure interaction analysis. This effective tool in fracture analyses should be complemented by traditional fractographic methods, including (but not limited to) optical- and scanning electron-microscopy. The porosity quantification method detailed in this study proved to be a quick and thorough method. Through these combined complementary 2-D and 3-D methods, crack propagation was shown to occur almost exclusively at the glass–matrix interfaces and through pores, showing that the bonding of glass particles to the matrix polymer requires improvement and also that porosity should be eliminated or reduced in the preparation process. Additionally, sample homogeneity was shown to improve strength through arresting and deflecting crack-propagation.

The methodological development within this work is exploitable on related biomaterials and represents a new tool towards the rational characterisation, optimisation and design of novel materials for clinical service.

Acknowledgments This work was supported by grants ETT-489/2009 and TAMOP-4.2.1.B of Hungary as well as TET-SIN-CELL-THER grant supported by NKTH-A*STAR. The authors thank Professor Brian W. Darvell for initiating this project, Ms. Elke Van de Casteele from SkyScan for her help with nano CT imaging and Miss Tóbiás Edit, Mr. Szabó Bence and Gimesi Brigitte for help with

sample preparation. Technical University Materials laboratory staff Mark and Peter are gratefully acknowledged for technical support and discussion. GC Corporation (Japan) is also acknowledged for donation of the materials tested. KVT, GAC, IGC thank GIOCOMMS (Toronto/Budapest/Beijing) for supporting international researcher and student exchanges, in addition to the Centre for Advanced Functional Materials (CAFMaD) through the Higher Educational Funding Council for Wales (HEFCW) for personal support 2006-2011.

References

1. Crisp S, Wilson AD. Reactions in glass ionomer cements: I. Decomposition of the powder. J Dent Res. 1974;53:1408–13. doi:10.1177/00220345740530061901.
2. Mount GJ. Color Atlas of Glass Ionomer Cements. 3rd ed. London: Dunitz; 2002.
3. Nicholson JW. Glass ionomer dental cements: update. Mater Tech Adv Perf Mater. 2010;25:8–13. doi:10.1179/175355509X12614966220506.
4. Jonck LM, Grobbelaar CJ, Strating H. Biological evaluation of glass-ionomer cement (Ketac-O) as an interface material in total joint replacement: a screening test. Clin Mater. 1989;4:201–24. doi:10.1016/0267-6605(89)90030-9.
5. Brook IM, Hatton PV. Glass-ionomers: bioactive implant materials. Biomater. 1998;19:565–71. doi:10.1016/S0142-9612(98)00138-0.
6. Bauer M, Pytel J, Vona I, Gerlinger I. Combination of ionomer cement and bone graft for ossicular reconstruction. Eur Arch Otorhinolaryngology. 2007;264:1267–73. doi:10.1007/s00405-007-0367-0.
7. Hehl K, Schumann K, Beck C, Schottle W. Middle-ear surgery–glass ionomer cement at the incudostapedial joint. Laryngorhinootologie. 1989;68:490–2. doi:10.1055/s-2007-998383.
8. Dicks F, Zollner W. Practicability of glass ionomer cement for veterinary dental practice. Praktische Tierarzt. 1988;69:32–6.
9. Vujaskovic M, Karadzic B, Bacetic D. Histopathology of subcutaneous tissue reaction to endodontic root canal sealers. Acta Veterinaria (Beograd). 2011;61:327–36. doi:10.2298/AVB1103327V.
10. Davidson CL. Advances in glass-ionomer cements. J Appl Oral Sci. 2006;14(sp. issue):3–9. doi:10.1590/S1678-77572006000700002.
11. Ten Cate JM, van Duinen RNB. Hypermineralization of dentinal lesions adjacent to glass-ionomer cement restorations. J Dent Res. 1995;74:1266–71. doi:10.1177/00220345950740060501.
12. Hotz P, McLean JW, Sced I, Wilson AD. The bonding of glass-ionomer cements to metal and tooth substrates. Brit Dent J. 1977;142:41–7. doi:10.1038/sj.bdj.4803864.
13. Powis DR, Folleras T, Merson SA, Wilson AD. Improved adhesion of a glass ionomer cement to dentin and enamel. J Dent Res. 1982;61:1416–22.
14. McLean JW, Wilson AD. The clinical development of the glass-ionomer cements. I. Formulations and properties. Aus Dent J. 1977;22:31–6. doi:10.1111/j.1834-7819.1977.tb04441.x.
15. McCabe JF, Yan ZQ, Al Naimi OT, Mahmoud G, Rolland SL. Smart materials in dentistry–future prospects. Dent Mater J. 2009;28:37–43. doi:10.4012/dmj.28.37.
16. McLean JW, Wilson AD. The clinical development of the glass-ionomer cement. II. Some clinical applications. Aus Dent J. 1977;22:120–7. doi:10.1111/j.1834-7819.1977.tb04463.x.
17. Lloyd CH, Mitchell L. The fracture toughness of tooth coloured restorative materials. J Oral Rehabil. 1984;11:257–72. doi:10.1111/j.1365-2842.1984.tb00575.x.
18. Crisp S, Pringuer MA, Wardleworth D, Wilson AD. Reactions in glass-ionomer cements: II An infrared spectroscopic study. J Dent Res. 1974;53:1414–9. doi:10.1177/00220345740530062001.
19. Crisp S, Wilson AD. Reactions in glass-ionomer cements: III. The precipitation reaction. J Dent Res. 1974;53:1420–4. doi:10.1177/00220345740530062101.
20. Wasson EA, Nicholson JW. New aspects of the setting of glass-ionomer cements. J Dent Res. 1993;72:481–3. doi:10.1177/00220345930720020201.
21. Nicholson JW. Chemistry of glass-ionomer cements: a review. Biomater. 1998;19:485–94. doi:10.1016/S0142-9612(97)00128-2.
22. Stamboulis A, Law RV, Hill RG. Characterisation of commercial ionomer glasses using magic angle nuclear magnetic resonance (MAS-NMR). Biomater. 2004;25:3907–13. doi:10.1016/j.biomaterials.2003.10.074.
23. Culbertson BM. New polymeric materials for use in glass-ionomer cements. J Dent. 2006;34:556–65. doi:10.1016/j.jdent.2005.08.008.
24. Kelly JR. Clinically relevant approach to failure testing of all-ceramic restorations. J Prosthet Dent. 1999;81:652–61. doi:10.1016/S0022-3913(99)70103-4.
25. Wang Y, Darvell BW. Failure mode of dental restorative materials under Hertzian indentation. Dent Mater. 2007;23:1236–44. doi:10.1016/j.dental.2006.11.016.
26. Crisp S, Lewis BG, Wilson AD. Characterization of glass-ionomer cements. 3. Effect of polyacid concentration on the physical properties. J Dent. 1977;5:51–6. doi:10.1016/S0300-5712(77)80025-0.
27. Hill RG, Wilson AD, Warrens CP. The influence of poly (acrylic acid) molecular weight on the fracture toughness of glass-ionomer cements. J Mater Sci. 1989;24:363–71. doi:10.1007/BF00660982.
28. Kajiwara M. Formation and compressive strength of the ionomer cements prepared from aluminosilicate glass and poly (acrylic acid). J Mater Sci Lett. 1984;3:617–9. doi:10.1007/BF00719627.
29. Quinn JB, Quinn GD. Material properties and fractography of an indirect dental resin composite. Dent Mater. 2010;26:589–99. doi:10.1016/j.dental.2010.02.008.
30. Scherrer SS, Kelly JR, Quinn GD, Xu K. Fracture toughness (K_{IC}) of a dental porcelain determined by fractographic analysis. Dent Mater. 1999;15:342–8. doi:10.1016/S0109-5641(99)00055-X.
31. Landis EN, Nagy EN, Keane DT. Microstructure and fracture in three dimensions. Eng Fract Mech. 2003;70:911–25. doi:10.1016/S0013-7944(02)00157-1.
32. Sinnett-Jones PE, Browne M, Ludwig W, Buffiere JY, Sinclair I. Microtomography assessment of failure in acrylic bone cement. Biomater. 2005;26:6460–6. doi:10.1016/j.biomaterials.2005.04.064.
33. Wang Y, Darvell BW. Interactive effect of indenter size and sample thickness in Hertzian indentation test. Dent Mater. 2010;26:539–44. doi:10.1016/j.dental.2010.02.001.
34. Bontaz-Carion J, Pellegrini YP. X-ray microtomography analysis of dynamic damage in tantalum. Adv Eng Mater. 2006;8:480–6. doi:10.1002/adem.200600058.
35. Nomoto R, Komoriyama M, McCabe JF, Hirano S. Effect of mixing method on the porosity of encapsulated glass ionomer cement. Dent Mater. 2004;20:972–8. doi:10.1016/j.dental.2004.03.001.
36. Deb S, Shah P, Vazquez B, San Roman J. A novel acrylic copolymer for a poly(alkenoate) glass-ionomer cement. J Mater Sci Mater Med. 2003;14:575–81. doi:10.1023/A:1024062705439.
37. Landis E, Keane DT. X-ray microtomography for fracture studies in cement-based materials. Development in X-ray Tomography II. Bonse (Ed.). Bellingham, WA. SPIE; 1999. SPIE Proc Vol 3772: 105-113. Cited by Stock SR, Microcomputed tomography: methodology and applications. Boca Raton: CRC press; 2008.

38. Goldman M. Fracture properties of composite and glass ionomer dental restorative materials. J Biomed Mater Res. 1985;19: 771–83. doi:10.1002/jbm.820190705.

39. Hull D. Fractography: Observing, measuring and interpreting fracture surface topography. Cambridge: University Press; 1999. p. 121–9.